

Cite this: *Mater. Adv.*, 2025,  
6, 5045

# Development of a colorimetric sensor utilizing itaconic acid-mediated Griess reaction for sensitive detection of nitrite and nitrate in agricultural products†

Anubhab Das, Sindhu I Sanakal, Gomathi Sivakumar, Anashwara Babu and Samarendra Maji \*

The presence of nitrite ( $\text{NO}_2^-$ ) and nitrate ( $\text{NO}_3^-$ ) in agricultural products causes significant health risks, highlighting the need for sensitive and selective detection methods. In this study, we developed a colorimetric sensor based on the Griess assay under organic acidic conditions to detect these compounds, where the formation of a pink color suggests the presence of  $\text{NO}_2^-$  and  $\text{NO}_3^-$ . We synthesized 4-aminobenzenesulfonohydrazide (**C**) and 2-(2-(naphthalen-1-ylamino)ethoxy)ethanol (**E**). *N*-(1-Naphthyl)ethylenediamine dihydrochloride (**F**), and commercially available organic dicarboxylic acid “itaconic acid” was used for the investigation. Two chemosensors were designed, one with compounds **C** and **E** (known as CE) and another containing compounds **C** and **F** (known as CF). These two chemosensors formed pink azo-dyes in the presence of  $\text{NO}_2^-$  in acidic conditions (using itaconic acid). The sensing ability was evaluated using UV-spectroscopy, and different sensitivity was demonstrated for the analyte ( $\text{NO}_2^-$ ). The binding constants for sensors CE and CF were determined to be  $5.06 \times 10^{-4} \text{ M}^{-1}$  and  $16.7 \times 10^{-4} \text{ M}^{-1}$ , respectively, based on the Benesi–Hildebrand (B–H) plot. Under the optimized conditions, chemosensor CE showed a linear range of 0.005–0.421 mM with a detection limit (LOD) of 0.62 mM, while chemosensor CF exhibited a range of 0.01–0.453 mM with a LOD of 0.52 mM. A smartphone-assisted  $\text{NO}_2^-$  sensing device was designed based on the RGB value of the generated pink color, which demonstrates the sensor's ability towards real-time detection of  $\text{NO}_2^-$  ions. Additionally, the system was extended to paper-based test strips for on-site detection. Our proposed sensor system is also capable of detecting  $\text{NO}_3^-$  by using Zn dust as a reducing agent to convert  $\text{NO}_3^-$  to  $\text{NO}_2^-$ . Real sample testing demonstrated excellent recovery, confirming the potential of this colorimetric sensor for  $\text{NO}_2^-$  and  $\text{NO}_3^-$  detection in agricultural products.

Received 3rd April 2025,  
Accepted 9th June 2025

DOI: 10.1039/d5ma00314h

rsc.li/materials-advances

## 1. Introduction

Nitrite ( $\text{NO}_2^-$ ) and nitrate ( $\text{NO}_3^-$ ) are naturally occurring nitrogen-containing compounds that play crucial roles in the biological nitrogen cycle, ensuring the recycling of nitrogen within ecosystems.<sup>1</sup> They are produced through nitrification, a process where nitrifying bacteria first oxidize ammonia ( $\text{NH}_3$ ) or ammonium ( $\text{NH}_4^+$ ) into  $\text{NO}_2^-$ , followed by the conversion of  $\text{NO}_2^-$  into  $\text{NO}_3^-$ .  $\text{NO}_3^-$ , being highly soluble and bioavailable, serves as a crucial nitrogen source for plants, which assimilate it to synthesize essential biomolecules such as amino acids,

proteins, and nucleotides. In oxygen-deprived environments,  $\text{NO}_3^-$  and  $\text{NO}_2^-$  undergo denitrification, where denitrifying bacteria convert them back into gaseous nitrogen or nitrous oxide, returning nitrogen to the atmosphere and maintaining ecological balance. These compounds act as intermediates in nitrogen transformations, adapting to environmental conditions to regulate nitrogen availability.<sup>2,3</sup> From various sources,  $\text{NO}_3^-$  and  $\text{NO}_2^-$  can enter the human body *via* different pathways. Vegetables play a significant role in absorbing these compounds from soil and water, especially in areas where nitrogen-based fertilizers or organic and livestock waste are heavily used.<sup>4</sup> Drinking water contaminated with agricultural runoff is another major contributor. Additionally, processed meats like bacon, sausages, and ham often contain added  $\text{NO}_2^-$  as a preservative and color stabilizer.<sup>5,6</sup> The Joint Food and Agricultural Organization/World Health Organization (WHO) has set an acceptable daily intake (ADI) of 3.7 mg of  $\text{NO}_3^-$  ion

Department of Chemistry, SRM Institute of Science and Technology, Kattankulathur, 603203, Tamilnadu, India. E-mail: samarenr@srmist.edu.in

† Electronic supplementary information (ESI) available: Structural characterization of B, C and E; visual color change, UV-vis, temperature stability study, DFT, test-strip, real-time application, and comparison study. See DOI: <https://doi.org/10.1039/d5ma00314h>



per kg of body weight and 0.06 mg of  $\text{NO}_2^-$  ion per kg of body weight.<sup>7,8</sup> To a certain level,  $\text{NO}_3^-$  intake is good as it has some positive effects like improving blood flow, reducing blood pressure, and cardio and vasoprotective effects.<sup>9–11</sup>  $\text{NO}_2^-$  helps to control and inhibit the growth of pathogenic bacteria, e.g., *Clostridium botulinum* and *Listeria monocytogenes*.<sup>12,13</sup> Besides, it acts as an antioxidant against lipid oxidation as well.<sup>14</sup>

However, excessive exposure to  $\text{NO}_2^-$  or  $\text{NO}_3^-$  beyond the aforementioned limit can cause significant health risks to humans. In the stomach,  $\text{NO}_2^-$  can combine with amines and amides to produce nitrosamines, which are strong carcinogens associated with a higher risk of gastrointestinal cancers.<sup>15,16</sup> High levels of  $\text{NO}_2^-$  can also cause methemoglobinemia, a condition that impairs the blood's ability to carry oxygen, leading to cyanosis or “blue baby syndrome” in infants.<sup>17–19</sup> Prolonged exposure to elevated  $\text{NO}_3^-$  and  $\text{NO}_2^-$  levels has been associated with adverse effects on thyroid function and a higher risk of cardiovascular diseases, pulse acceleration, muscular tremors, dyspnoea, cyanosis and vomiting, and can even cause death in extreme cases.<sup>20</sup> Due to the widespread recognition of these problems, the majority of developed nations have put in place legal frameworks designed to control their levels in food and environmental products. Therefore, the daily routine examination of  $\text{NO}_3^-$  or  $\text{NO}_2^-$  in agricultural products is necessary for safety and quality management.

Several strategies have been developed to detect  $\text{NO}_3^-$  and  $\text{NO}_2^-$  accurately due to their environmental and health implications. Scientists have explored a variety of advanced methods, including electrochemical techniques,<sup>21,22</sup> which involve measuring the electrical response of  $\text{NO}_3^-$  or  $\text{NO}_2^-$  in a solution, and potentiometry, which uses ion-selective electrodes to determine their concentrations.<sup>23</sup> Conductometry is also a method by which these ions are detected by the changes in electrical conductivity due to the presence of  $\text{NO}_3^-$  and  $\text{NO}_2^-$ .<sup>24</sup> Spectroscopic techniques, such as UV-visible and infrared spectroscopy, enable qualitative and quantitative analysis based on light absorption or emission properties.<sup>25,26</sup> Ion chromatography and high-performance liquid chromatography (HPLC) are widely utilized for their ability to separate and quantify  $\text{NO}_3^-$  and  $\text{NO}_2^-$  in complex mixtures,<sup>27,28</sup> while gas chromatography-mass spectrometry (GC-MS) provides high sensitivity and specificity in detection.<sup>29</sup> The chemiluminescence method, relying on light emission during chemical reactions, has also been effectively employed.<sup>30</sup> Enzyme-based detection methods have gained attention for their specificity, particularly in detecting  $\text{NO}_3^-$  through enzymatic reactions.<sup>31</sup> Similarly, capillary electrophoresis has proven to be a reliable technique for quantifying both  $\text{NO}_3^-$  and  $\text{NO}_2^-$  due to its high resolution and efficiency.<sup>32</sup> Despite their effectiveness, these techniques have intrinsic limitations, such as high operational costs, time-consuming procedures, and the need for skilled personnel, which hinder their practical application in field settings. Given these challenges, researchers have sought alternative approaches with greater simplicity, sensitivity, and selectivity. Among these,

colorimetric detection using the Griess reagent has stood out as a straightforward and widely applied method. This approach, which has been used for over a century, relies on a color change reaction to visually or spectrophotometrically determine  $\text{NO}_2^-$  or  $\text{NO}_3^-$  concentrations, offering a cost-effective and practical solution for routine analysis.<sup>33</sup>

The Griess reaction, first reported in 1879, is a well-established chemical method for detecting  $\text{NO}_2^-$  and indirectly  $\text{NO}_3^-$  in various samples. This reaction employs two reagents, sulfanilamide and *N*-(1-naphthyl)ethylenediamine dihydrochloride (NED), under acidic conditions. Initially, sulfanilamide reacts with  $\text{NO}_2^-$  in the Griess diazotization reaction to form an electrophilic diazonium salt. This intermediate subsequently undergoes an azo coupling reaction with NED to produce an intensely colored azo dye, characterized by the functional group  $\text{R-N=N-R}'$ . Due to its simplicity and effectiveness, the Griess assay has remained the most widely used colorimetric method for  $\text{NO}_2^-$  detection for over a century.<sup>34–38</sup> Capitán-Vallvey and coworkers developed  $\text{NO}_2^-$  detecting test strips based on the Griess assay under acidic conditions, demonstrating their application for detecting  $\text{NO}_2^-$  in various water sources, including spring, mineral, tap, well, and seawater.<sup>39</sup> Wu and coworkers designed a dual-readout sensor by conjugating carbon dots with 3-aminophenol, offering both colorimetric and fluorescent detection for  $\text{NO}_2^-$  with detection limits of 10 nM and 2.5  $\mu\text{M}$ , respectively.<sup>40</sup> Furthermore, polydimethylsiloxane (PDMS)-based microfluidic devices have been employed to detect  $\text{NO}_2^-$  in meat samples with a limit of detection (LOD) of 0.1  $\text{mg L}^{-1}$ .<sup>41</sup> Detection of  $\text{NO}_3^-$  using the Griess assay requires an additional reduction step to convert  $\text{NO}_3^-$  into  $\text{NO}_2^-$ . This reduction is typically performed using metals such as cadmium (Cd) or zinc (Zn) under acidic conditions, following the reaction mechanism:  $\text{NO}_3^- + \text{M(s)} + 2\text{H}^+ \rightarrow \text{NO}_2^- + \text{M}^{2+} + \text{H}_2\text{O}$ .<sup>42</sup> Zn is preferred due to its lower toxicity, affordability, and eco-friendly properties. Murray and coworkers designed a portable  $\text{NO}_3^-$  detection system by coupling Zn powder with the Griess assay.<sup>43,44</sup> Pai *et al.* introduced vanadium as a reducing agent for  $\text{NO}_3^-$ , combining it with the Griess reagent to design a sensor capable of detecting both  $\text{NO}_3^-$  and  $\text{NO}_2^-$ , achieving a LOD of 0.2  $\mu\text{M}$ .<sup>45</sup> Polymer-based adaptations of the Griess test have also been reported.<sup>41,46</sup> A Griess reagent-doped hydrogel test kit and a Zn powder-doped starch film were developed to quantify  $\text{NO}_2^-$  and  $\text{NO}_3^-$ , exhibiting LODs of 50  $\mu\text{g L}^{-1}$  for  $\text{NO}_2^-$  and 0.32  $\mu\text{g L}^{-1}$  for  $\text{NO}_3^-$ , respectively.<sup>37</sup> These advancements demonstrate the versatility and adaptability of the Griess reaction for diverse applications in  $\text{NO}_2^-$  and  $\text{NO}_3^-$  detection.

In these reported approaches, mineral acid (e.g., HCl) has been used as the source of acid in the Griess test. However, the toxic nature of mineral acid affects the environment. These shortcomings can be overcome by using organic acid. Organic acids' lower-toxicity and milder activity make them environmentally sustainable and applicable in food and beverage applications. Itaconic acid is a popular organic acid and an unsaturated dicarboxylic acid with a methylene group connected to one carboxyl group. It has huge applications in the agro-based, plastics, textile, paint and pharmaceutical sectors.<sup>47</sup>



Furthermore, none of the studies examine the use of itaconic acid as the acid source in test strip-based sensors or smartphone-based sensors to cover both  $\text{NO}_2^-$  and  $\text{NO}_3^-$  in a single report. In our present study, we developed two chemosensors (CE and CF) for the colorimetric detection of  $\text{NO}_2^-$  and  $\text{NO}_3^-$ . These systems were designed using itaconic acid as the acidic component, and their functionality was based on the principles of the Griess assay. Both sensor systems demonstrated the capability to detect  $\text{NO}_2^-$ , with results observable either visually through a distinct color change or quantitatively using UV-visible spectroscopy. To evaluate the practicality of the proposed sensors, trace amounts of  $\text{NO}_2^-$  were successfully detected in real-world samples, including various vegetables and lake water, demonstrating the system's reliability and applicability in diverse environments. Additionally, test strips were fabricated by coating the dye onto filter paper, which produced a vivid pink color upon exposure to  $\text{NO}_2^-$ , offering a simple and portable detection method. Furthermore, the system was extended for  $\text{NO}_3^-$  detection by incorporating a reduction step using Zn dust. In this process,  $\text{NO}_3^-$  was reduced to  $\text{NO}_2^-$ , enabling the sensor to detect  $\text{NO}_3^-$  indirectly while maintaining a high level of responsiveness and accuracy. These results highlight the versatility and effectiveness of the developed systems for  $\text{NO}_2^-$  and  $\text{NO}_3^-$  sensing in various applications.

## 2. Experimental

### 2.1. Materials

All solvents and chemicals used in this work were of analytical grade and used without further purification. *N*-Acetyl sulfonyl chloride was purchased from Sigma-Aldrich. *N*-(1-Naphthyl)-ethylenediamine dihydrochloride, itaconic acid (99% purity), 4-dimethylaminopyridine (DMAP), dichloromethane, activated basic aluminum oxide, silica gel, acetonitrile, hydrazine hydrate (80%), triethylamine (AR 99.5%), sodium oxalate, sodium hydroxide, sodium carbonate, sodium fluoride, sodium bromide, sodium sulfate, sodium iodide, sodium phosphate tribasic, sodium nitrate, and sodium chloride were obtained from Sisco Research Laboratories Pvt. Ltd (SRL), Maharashtra, India. 1-Naphthylamine was purchased from TCI Chemicals (India) Pvt. Ltd. Sodium nitrite and hydrochloric acid, hexane (Hex), ethyl acetate (EA), and chloroform were obtained from Avantor Performance Materials India Limited, Maharashtra, India. 1-*n*-Butyl-3-methylimidazoliumtetrafluoroborate (98% purity) ([BMIM]BF<sub>4</sub>) was sourced from Thermo Fisher Scientific India Pvt. Ltd, Mumbai. Methanol was obtained from Advent Chembio Pvt. Ltd, and Milli-Q water was used throughout the experiments.

### 2.2. Characterization

<sup>1</sup>H-NMR spectra were recorded on a Bruker Advance 500 MHz spectrometer in chloroform-*d* (CDCl<sub>3</sub>), purchased from Eurisotop, at room temperature. Chemical shifts ( $\delta$ ) are reported in parts per million (ppm), relative to CDCl<sub>3</sub> at 7.24 ppm. Fourier

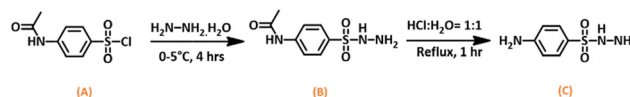
transform infrared (FT-IR) spectra were acquired using a Shimadzu IR Tracer-100 in the attenuated total reflectance (ATR) mode, covering the 400–4000 cm<sup>-1</sup> range. LC-MS analysis was performed on an LC-MS 2020 system equipped with an LC10ADVP Binary pump (Shimadzu, Japan). UV-vis absorption spectra were recorded in water using an Agilent Cary 5000 double-beam UV-vis spectrometer. Ground and excited states were optimized using density functional theory (DFT) with the B3LYP/6-31G and LANL2DZ basis sets. RGB values were calculated using the RGB Detector app on an Android OS to determine the LOD.

### 2.3. Synthesis

**2.3.1. Preparation of 4-aminobenzenesulfonylhydrazide (C).** Compound 4-aminobenzenesulfonylhydrazide (C) was synthesized in a two-step process mentioned in Scheme 1. *N*-(4-(Hydrazinylsulfonyl)phenyl)acetamide (B) was synthesized following the reported method with slight modification.<sup>48</sup> *N*-Acetyl sulfonyl chloride (A) (20.0 g, 0.086 mol) was added in portions to 100 mL (2.04 mol) hydrazine hydrate cooled to 0 °C in an ice bath. The mixture was allowed to warm up to 5 °C, stirred for 4 h, and poured into water, and the precipitate was filtered off and dried for 24 h in the air until constant weight, which provided 12.78 g of compound with 65% yield. <sup>1</sup>H NMR of the compound (B) is shown in Fig. S1 (ESI<sup>†</sup>). <sup>1</sup>H NMR (500 MHz, DMSO-*d*<sub>6</sub>): 2.09 (s, 3H), 4.04 (s, 2H), 7.72 (d, 2H), 7.75 (d, 2H), 8.24 (s, 1H), 10.33 (s, 1H). FTIR ( $\lambda_{\text{max}}$ , cm<sup>-1</sup>): 1395, 1521, 1578, 1672, 2859, 3226 and 3320 (Fig. S2, ESI<sup>†</sup>). LC-MS MS (*m/z*): [M - H]<sup>+</sup> = 228.05 (calculated); 227.9 (observed) (Fig. S3, ESI<sup>†</sup>).

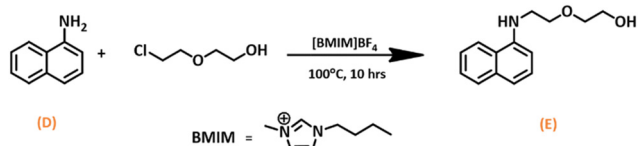
Next, compound 4-aminobenzenesulfonylhydrazide (C) was prepared as a previously reported method.<sup>46</sup> Compound (B) (7.8 g, 0.034 mol) was dissolved in a 25 mL 1 : 1 mixture of H<sub>2</sub>O and conc. HCl in a round-bottom flask, and the reaction mixture was refluxed for 1.5 h. After cooling to room temperature, the mixture was neutralized by the gradual addition of solid sodium bicarbonate until effervescence ceased. The solution was then placed on ice to facilitate precipitation. The resulting precipitate was filtered and dried until constant weight to get 0.89 g of product with a yield of 14%. <sup>1</sup>H NMR of the compound (C) is shown in Fig. S4 (ESI<sup>†</sup>). <sup>1</sup>H NMR (500 MHz, DMSO-*d*<sub>6</sub>): 1.77 (m, 3H), 5.93 (s, 2H), 6.56 (d, 2H), 7.43 (d, 2H). FTIR ( $\lambda_{\text{max}}$ , cm<sup>-1</sup>): 686, 1084, 1156, 2900, 3200, 3333, and 3470 (Fig. S5, ESI<sup>†</sup>). LC-MS (*m/z*): [M + H]<sup>+</sup> = 188 (calculated); 187.6 (observed) (Fig. S6, ESI<sup>†</sup>).

**2.3.2. Synthesis of 2-(2-(naphthalen-1-ylamino)ethoxy)ethanol (E).** 2-(2-(Naphthalen-1-ylamino)ethoxy)ethanol (E) was synthesized *via* a single-step procedure as shown in Scheme 2. The monosubstituted product was obtained using an ionic liquid catalyst following the procedure described in the



Scheme 1 Synthetic scheme for the synthesis of compound (C).





Scheme 2 A schematic representation of compound (E) synthesis using an ionic liquid approach.

literature.<sup>49</sup> Ethyleneglycolmono-2-chloroethylether (13.1 g, 0.105 mol) was added to a mixture of 1-naphthalamine (D) (5 g, 0.035 mol) in [BMIM]BF<sub>4</sub> (0.225 g, 0.001 mol). After addition, the reaction was stirred for 12 h at 100 °C. After the completion of the reaction, the reaction mixture was extracted with ethyl acetate, and compound (H) was purified by column chromatography using EA/Hex to obtain the desired compound (E) (yield: 3.5 g, 45%). <sup>1</sup>H NMR of the compound (E) is shown in Fig. S7 (ESI<sup>†</sup>). <sup>1</sup>H NMR (500 MHz, CDCl<sub>3</sub>): 3.45 (t, 2H), 3.61 (m, 2H), 3.75 (m, 2H), 3.83 (t, 2H), 7.24 (d, 1H), 7.34 (t, 1H), 7.43 (m, 2H), 7.78 (m, 1H), 7.84 (m, 1H). FTIR ( $\lambda_{\text{max}}$ , cm<sup>-1</sup>): 1050, 1575, 2857, and 3376 (Fig. S8, ESI<sup>†</sup>). LC-MS ( $m/z$ ): [M + H]<sup>+</sup> = 232.13 (calculated); 232.15 (observed) (Fig. S9, ESI<sup>†</sup>).

#### 2.4. Preparation of the real sample

The real sample was brought from a nearby supermarket. The sample was prepared according to the procedure mentioned in the literature with a slight modification.<sup>50</sup> All vegetables were cleaned properly. The root vegetables were peeled to remove possible traces of soil. The entire mass of the sample was homogenized with a blender. 1.0 g of homogenized sample was extracted with 10 mL MeOH:H<sub>2</sub>O = 1:1 extraction solution, followed by ultrasonication for 15 minutes. The extracted solution was diluted over 20 times and filtered through a 0.45  $\mu\text{m}$  syringe filter. The lake water and tap water were directly filtered through a 0.45  $\mu\text{m}$  syringe filter. Finally, real samples were obtained after the stock solution was spiked with various concentrations of NO<sub>2</sub><sup>-</sup>.

#### 2.5. Sensing procedure

The NO<sub>2</sub><sup>-</sup> sensing study was conducted at room temperature. A standard stock solution (5 mM) of NO<sub>2</sub><sup>-</sup> was prepared by dissolving the appropriate amount of NO<sub>2</sub><sup>-</sup> salt in an aqueous solution. Interference study was checked by fluoride (F<sup>-</sup>), chloride (Cl<sup>-</sup>), bromide (Br<sup>-</sup>), iodide (I<sup>-</sup>), oxalate (C<sub>2</sub>O<sub>4</sub><sup>2-</sup>), phosphate (PO<sub>4</sub><sup>3-</sup>), carbonate (CO<sub>3</sub><sup>2-</sup>), nitrate (NO<sub>3</sub><sup>-</sup>), hydroxide (OH<sup>-</sup>), and sulfate (SO<sub>4</sub><sup>2-</sup>) anions and corresponding stock solutions (5 mM) were prepared. Itaconic acid was used as the acid source. Combinations of sensor compounds, specifically (C) with (E) (sensor CE) and (C) with (F) (sensor CF), were prepared in an aqueous solution (10 mL, 1 mM) by stirring for 30 minutes. A 10 mM itaconic acid solution (10 mL) was also prepared in water. An equivalent mixture of both dyes (0.5 mL) and itaconic acid (0.5 mL) was placed in a cuvette, followed by the addition of 1 mL of water. The UV-vis spectra of this mixture were recorded over a wavelength range of 200 to 800 nm. Following the same procedure, NO<sub>3</sub><sup>-</sup> was detected using Zn

dust (1 mg) and 1N HCl (5  $\mu\text{L}$ ) as a reducing agent. Here, in addition to itaconic acid, 1N HCl (5  $\mu\text{L}$ ) was also used as it helps in the reduction process.

## 3. Results and discussion

### 3.1. Synthesis and characterization of 4-aminobenzenesulfonylhydrazide (C) and 2-(2-(naphthalen-1-ylamino)ethoxy)ethanol (E)

The compound (C) was synthesized by a two-step procedure as previously reported with slight modifications (Scheme 1).<sup>46</sup> The first step is the hydrazination of the starting materials of (A) in the presence of hydrazine hydrate, followed by the deprotection of the *N*-acetyl group in an acid medium to obtain (C). The structure of (C) was confirmed by <sup>1</sup>H NMR spectroscopy (Fig. S4, ESI<sup>†</sup>), where the multiplet peak arises at  $\delta$  1.77 due to three protons present next to the -SO<sub>2</sub> group, and the singlet peak at  $\delta$  5.93 ppm due to two amine hydrogens next to the phenyl ring. Four aromatic protons are exhibited, corresponding to a doublet peak at  $\delta$  6.56 and 7.43 ppm. The deprotection was confirmed by the vanishing of the acetyl (-COCH<sub>3</sub>) protons' peak at 2.09 ppm (Fig. S4, ESI<sup>†</sup>), which was present in Fig. S1 (ESI<sup>†</sup>). Additionally, the mass  $m/z$  peak at 187.7 confirms the formation of (C) (Fig. S7, ESI<sup>†</sup>).

Compound (E) was designed and synthesized *via* a single-step process. The starting compound (D) was reacted with ligand ethyleneglycolmono-2-chloroethylether to form the mono-substituted product (E), catalyzed by ionic liquid [BMIM]BF<sub>4</sub>. The formation of the compound was proven by <sup>1</sup>H NMR spectroscopy (Fig. S7, ESI<sup>†</sup>). Four pairs of proton peaks were exhibited at  $\delta$  3.45, 3.61, 3.75, and 3.83 ppm, respectively. The seven aromatic protons were observed at  $\delta$  7.24–7.84 ppm. The mass  $m/z$  peak at 232.15 confirms the successful formation of (E) (Fig. S9, ESI<sup>†</sup>).

### 3.2. Colorimetric sensing of NO<sub>2</sub><sup>-</sup>

The absorption spectra of the chemosensor (CE) were recorded in the presence of NO<sub>2</sub><sup>-</sup>, as shown in Fig. 1a. No peak was formed at 530 nm in the absence of NO<sub>2</sub><sup>-</sup>. However, after the incubation of NO<sub>2</sub><sup>-</sup>, a new peak at 530 nm was generated due to the formation of the diazo compound, and gradually, the intensity of the peak was increased with the increase of NO<sub>2</sub><sup>-</sup> concentration. The results support the visual observations shown in Fig. S10 (ESI<sup>†</sup>), demonstrating a color change in the sensor system from colorless to pink. The system has shown an enhancement of absorbance for NO<sub>2</sub><sup>-</sup> concentration in the range of 0.005 to 0.421 mM. However, with the further addition of NO<sub>2</sub><sup>-</sup>, a reduction in absorbance was observed, notably at a concentration around  $\sim$ 0.47 mM. As indicated in Fig. S11 (ESI<sup>†</sup>), a pink color solution was observed up to 0.421 mM of NO<sub>2</sub><sup>-</sup> (Fig. S11a, ESI<sup>†</sup>), followed by a yellow color solution at 0.842 mM. This might be owing to the development of the azo-dye complex, whose concentration increases with the addition of NO<sub>2</sub><sup>-</sup>, and which is thought to be destabilized due to the dye's reduced solubility and the dyes' predominant



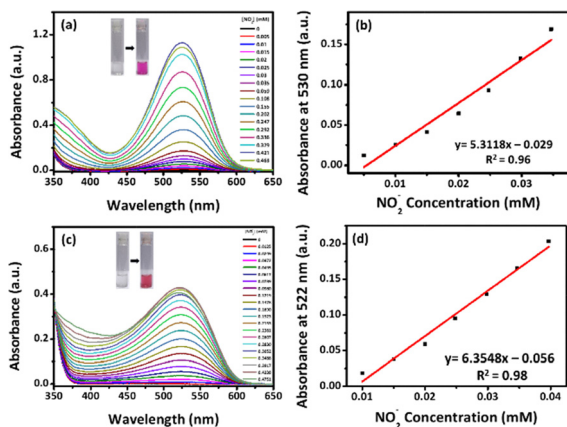


**Fig. 1** (a) UV-visible titration spectra of chemosensor CE (concentration of each dye is 0.25 mM and concentration of itaconic acid is 2.5 mM) with various concentrations of  $\text{NO}_2^-$  (0–0.46 mM) and (b) corresponding calibration response for the determination of  $\text{NO}_2^-$ , (c) UV-vis absorption spectra of chemosensor CF (concentration of each dye is 0.25 mM and concentration of itaconic acid is 2.5 mM) with various concentrations of  $\text{NO}_2^-$  (0–0.47 mM) and (d) corresponding calibration response towards  $\text{NO}_2^-$  determination.

hydrophobic interaction in the investigating aqueous medium. The absorbance value demonstrated a good linear range of 0.005–0.0347 mM (Fig. 1b). The regression equation is  $A = 5.3118 \text{ (mM)} - 0.029$  with a correlation coefficient of 0.96. The LOD was calculated using the following equation (eqn (1)) and found to be 0.62 mM.

$$\text{LOD} = 3.3 \times \sigma/S \quad (1)$$

where  $\sigma$  = the standard deviation of the response and  $S$  = the slope of the calibration curve.

Similarly, the chemosensor (CF) (Fig. 1c) showed a peak at 522 nm upon interaction with  $\text{NO}_2^-$ , confirming the formation of the azo dye compound. The results support the visual observations shown in Fig. S12 (ESI<sup>†</sup>), demonstrating a color change in the sensor system from colorless to pink. The absorbance increased linearly within the range of 0.01–0.0397 mM (Fig. 1d), with the regression equation  $A = 6.3548 \text{ (mM)} - 0.056$  and a correlation coefficient of 0.98. Similarly, (CF) demonstrated a reduction in absorbance at higher concentrations, particularly at 0.4751 mM, owing to the destabilization at higher concentrations of  $\text{NO}_2^-$  as discussed earlier (Fig. S11b, ESI<sup>†</sup>), where at the 0.88 mM  $\text{NO}_2^-$  concentration, the pink color solution turned yellow. The LOD for (CF) was calculated and found to be 0.52 mM.

Furthermore, the binding constant was calculated by using the Benesi–Hildebrand method (B–H plot), where a graph between  $1/(A_0 - A)$  and  $1/[\text{NO}_2^-]$  was plotted (Fig. 2) and a linear plot was obtained. The chemosensor (CE) demonstrated a binding constant of  $5.06 \times 10^{-4} \text{ M}^{-1}$  with  $R^2 = 0.985$  (Fig. 2a) and (CF) exhibited a binding constant value of  $16.7 \times 10^{-4} \text{ M}^{-1}$  with  $R^2 = 0.934$  (Fig. 2b).

The temperature and the long-term stability of the chemosensors were checked. The study was done by observing the

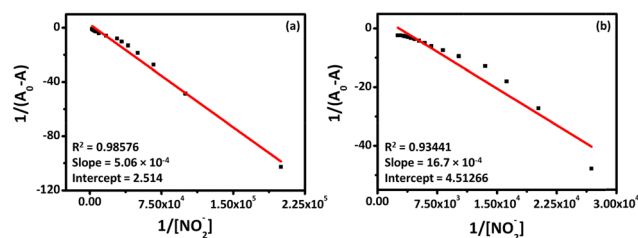


**Fig. 2** Benesi–Hildebrand plot of chemosensor (a) (CE) and (b) (CF) upon different concentrations of  $\text{NO}_2^-$  (0–0.4 mM).

change in the intensity of the peak that arises for both chemosensors with and without the presence of  $\text{NO}_2^-$ . Without the presence of the analyte, chemosensor (CE) exhibited an absorption peak at 324 nm, whereas (CF) showed an absorption peak at 319 nm (Fig. S13, ESI<sup>†</sup>). The temperature ranging from 25 to 50 °C was selected and the results are depicted in Fig. S14 (ESI<sup>†</sup>). The outcome demonstrated a slight increase in the intensity for sensor (CE), which may be due to the increase of solubility of the CE, whereas the intensity of sensor (CF) remains almost the same (Fig. S14a and c, ESI<sup>†</sup>).

The intensity of the nitrite detection peak corresponding to both sensors was reduced with the increase in temperature (Fig. S14b and d, ESI<sup>†</sup>). A prolonged stability test was done for 8 h (Fig. S15, ESI<sup>†</sup>). We have noticed some changes of UV-vis absorbance @530 nm for CE whereas, @522 nm for CF at the earlier stage of investigation. After 1 h, an unaltered intensity value was observed from 2–8 h for both sensors, which referred to the negligible change in sensitivity over time (Fig. S15a and c, ESI<sup>†</sup>). Therefore, we can conclude that both chemosensors were stable at that temperature and over a long time. However, the response in the presence of the analyte ( $\text{NO}_2^-$ ) needs to be observed quickly, as the intensity of the peak changes with temperature and time.

### 3.3. Selectivity and interference study

The selective colorimetric response of the proposed sensor systems to  $\text{NO}_2^-$  was evaluated by introducing various other anions ( $\text{F}^-$ ,  $\text{Cl}^-$ ,  $\text{Br}^-$ ,  $\text{I}^-$ ,  $\text{C}_2\text{O}_4^{2-}$ ,  $\text{PO}_4^{3-}$ ,  $\text{CO}_3^{2-}$ ,  $\text{NO}_3^-$ ,  $\text{OH}^-$  and  $\text{SO}_4^{2-}$ ). Both the chemosensors (CE) and (CF) exhibited high selectivity for  $\text{NO}_2^-$  detection. When  $\text{NO}_2^-$  was introduced, the chemosensor (CE) displayed a clear peak at 530 nm; however, no significant changes were observed for other anions (Fig. 3a and Fig. S16, ESI<sup>†</sup>). This was further validated by a histogram plot (Fig. 3b) showing enhanced absorbance at 530 nm exclusively for  $\text{NO}_2^-$  and a visible color change to pink, while other anions caused no color change (Fig. S17, ESI<sup>†</sup>). Similarly, the introduction of  $\text{NO}_2^-$  caused a clear peak at 522 nm in the chemosensor (CF), with no discernible alterations for the other anions (Fig. 3c and Fig. S18, ESI<sup>†</sup>). When  $\text{NO}_2^-$  was added, the (CF) chemosensor showed a selective pink color, similar to the (CE) chemosensor, however, other exploring anions did not exhibit any color change (Fig. S19, ESI<sup>†</sup>). The histogram plot for (CF) (Fig. 3d) confirmed this finding. These findings establish both systems as highly specific for  $\text{NO}_2^-$  detection.



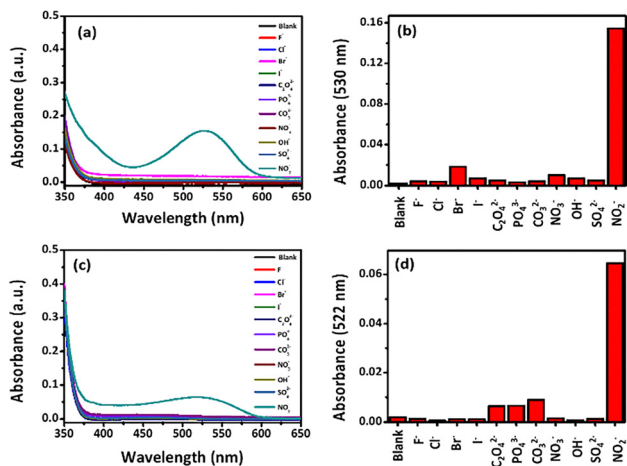


Fig. 3 (a) UV-vis spectra of the sensor (CE) with various anions, (b) corresponding absorption value at 530 nm presented in a bar diagram, (c) UV-vis spectra of the sensor (CF) with various anions and (d) corresponding absorption value at 522 nm presented in a bar diagram (concentration of each dye is 0.25 mM, concentration of itaconic acid is 2.5 mM and concentration of every anion is 0.349 mM).

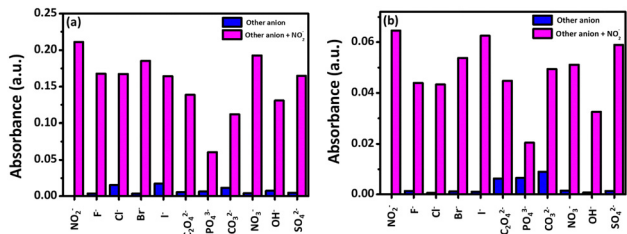


Fig. 4 Interference study of the sensor (a) (CE) and (b) (CF) in the presence of different anions.

Colorimetric readouts towards different anions were observed to check the interference study of our proposed sensors (Fig. 4).

Therefore, the competition experiment was carried out in the presence of  $\text{NO}_2^-$  (1 equiv.) mixed with other anions (1 equiv.) in aqueous solution. Different types of anions *viz.*  $\text{F}^-$ ,  $\text{Cl}^-$ ,  $\text{Br}^-$ ,  $\text{I}^-$ ,  $\text{C}_2\text{O}_4^{2-}$ ,  $\text{PO}_4^{3-}$ ,  $\text{CO}_3^{2-}$ ,  $\text{NO}_3^-$ ,  $\text{OH}^-$  and  $\text{SO}_4^{2-}$  were considered in order to investigate the interference study. According to observation, both sensors showed some interfering effects with  $\text{PO}_4^{3-}$  and  $\text{OH}^-$ . The interference observed in the proposed colorimetric sensor, particularly with  $\text{PO}_4^{3-}$  and  $\text{OH}^-$  ions, is primarily due to their impact on the system's acidity. The Griess reaction, which serves as the basis for the detection mechanism, requires an acidic environment to facilitate the efficient formation of the diazonium intermediate and the subsequent azo dye.  $\text{OH}^-$  ions, being strongly basic, neutralize protons ( $\text{H}^+$ ) in the solution, reducing the acidity and hindering the reaction. Similarly,  $\text{PO}_4^{3-}$  ions, though weaker bases, act as buffers that partially neutralize the acidic conditions, diluting the concentration of free  $\text{H}^+$  necessary for the reaction to proceed efficiently.

### 3.4. $\text{NO}_3^-$ detection

Our proposed sensor system is also capable of detecting  $\text{NO}_3^-$  by using Zn dust as a reducing agent to convert  $\text{NO}_3^-$  to  $\text{NO}_2^-$ ,



Scheme 3 Chemical reaction of reduction of  $\text{NO}_3^-$  in the presence of Zn dust.

which can then be detected by the proposed chemosensor (Scheme 3). To facilitate this reduction, HCl was used as the acid source, as metal reduction requires a strong acid. Eventually, similar to  $\text{NO}_2^-$ , sensor (CE) demonstrated the generation of a peak at 530 nm in the presence of  $\text{NO}_3^-$  (Fig. 5a). In contrast, the sensor (CF) exhibited a peak around 522 nm when exposed to  $\text{NO}_3^-$  (Fig. 5b).

The UV-vis spectra of the sensors at various  $\text{NO}_3^-$  concentrations were recorded under optimized conditions, and the LOD was calculated from the plot. For sensor (CE), the absorption at 530 nm increased gradually with  $\text{NO}_3^-$  concentration up to 0.412 mM (Fig. 5a), but a further increase in concentration (0.453 mM) led to a decrease in absorbance. A linear relationship was observed between absorption and  $\text{NO}_3^-$  concentration in the range of 0.005–0.326 mM (Fig. 5b). The regression equation is  $A = 1.14244 \text{ (mM)} - 0.04628$ , with a correlation coefficient of 0.98. The detection limit for  $\text{NO}_3^-$  was found to be 2.89 mM. Although it did not exhibit a linear calibration with  $\text{NO}_3^-$  concentration, the sensor (CF) responded to  $\text{NO}_3^-$  under similar situations (Fig. 5c and d).

The responsiveness of both sensors to a variety of ambient anions was assessed using colorimetric assays. As depicted in Fig. 6, none of these anions caused a significant change in the sensor (CE) (Fig. 6a and b) and sensor (CF) (Fig. 6c and d). Notably, only the sensor exposed to  $\text{NO}_3^-$  exhibited a color change to pink, while the other anions did not induce any observable color shift (Fig. S20 and S21, ESI<sup>†</sup>). The interference study assessed the sensors' performance in the presence of

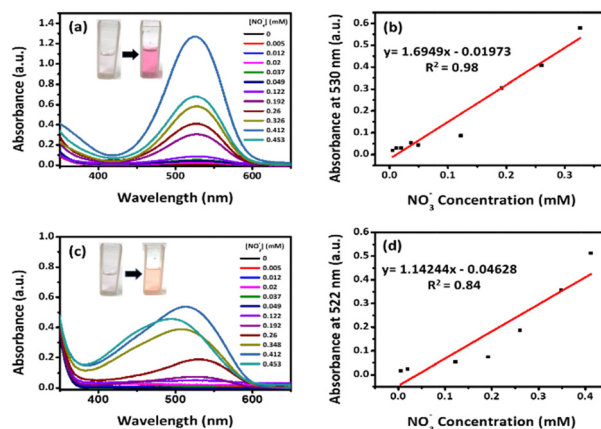


Fig. 5 (a) UV-vis titration spectra of the chemosensor (CE) (concentration of each dye is 0.25 mM, concentration of HCl is 2.5 mM and concentration of Zn dust is 1 mg/2 mL) with various concentrations of  $\text{NO}_3^-$  (0–0.453 mM) and (b) corresponding calibration response for the determination of  $\text{NO}_3^-$ , (c) UV-visible absorption spectra of the chemosensor (CF) (concentration of each dye is 0.25 mM, concentration of HCl is 2.5 mM and concentration of Zn dust is 1 mg/2 mL) with various concentrations of  $\text{NO}_3^-$  (0–0.453 mM) and (d) corresponding calibration response towards  $\text{NO}_3^-$  determination.



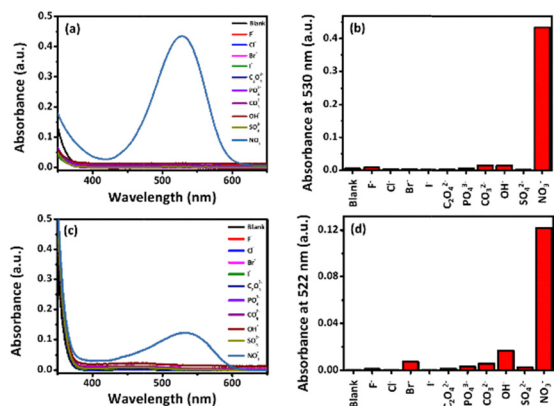


Fig. 6 (a) UV-vis spectra of the sensor (CE) with various anions, (b) corresponding absorption value at 530 nm presented in a bar diagram, (c) UV-vis spectra of the sensor CF with various anions and (d) corresponding absorption value at 522 nm presented in a bar diagram (concentration of each dye is 0.25 mM, concentration of HCl is 2.5 mM, concentration of every anion is 0.349 mM and 1 mg/2 mL of Zn dust was used).

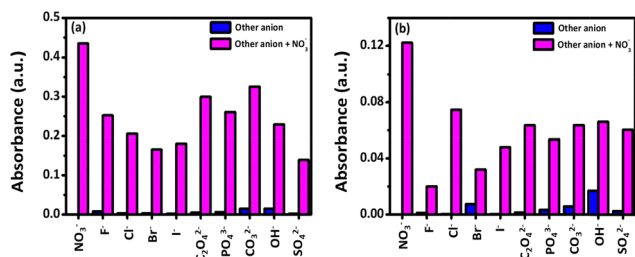


Fig. 7 Interference study of sensor (a) (CE) and (b) (CF) (with the presence of Zn dust as reducing agent) in the presence of other anions.

other anions by mixing  $\text{NO}_3^-$  (1 equiv.) with various anions (1 equiv.) in aqueous solution. The results, shown in Fig. 7, indicated that most anions interfered with  $\text{NO}_3^-$  detection. Sensor (CF) (Fig. 7b) was more affected by the presence of these anions than sensor (CE) (Fig. 7a).

### 3.5. Sensing mechanism

To investigate the sensing mechanism of the proposed chemosensors, their UV-vis absorption spectra were recorded. As shown in Fig. 8a, sensor (CE) exhibited a strong absorption peak at 530 nm exclusively upon the addition of  $\text{NO}_2^-$ , which confirms the formation of an azo compound. A similar spectral

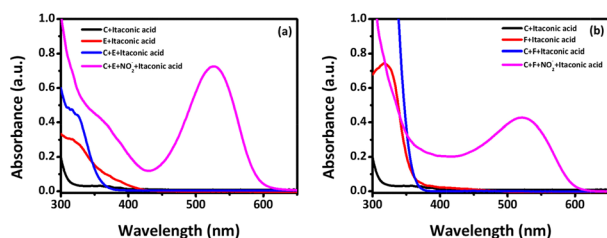
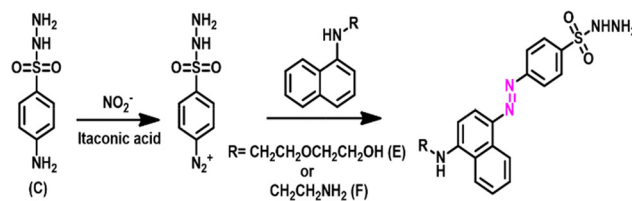


Fig. 8 UV-vis spectra of chemosensors (a) (CE) and (b) (CF) with the absence or presence of  $\text{NO}_2^-$ .



Scheme 4 Sensing scheme of our proposed system.

behavior was observed for sensor (CF), as represented in Fig. 8b.

The basic detection mechanism is based on the well-known Griess reaction.<sup>40</sup> In this system, compound (C), which possesses an aromatic amine ( $-\text{NH}_2$ ) and a sulfonohydrazide group, reacts with  $\text{NO}_2^-$  in the presence of itaconic acid to generate a diazonium salt. This intermediate then undergoes a coupling reaction with either compound (E) or (F) to form a pink-colored azo dye, as shown in Scheme 4.

The structural and electronic properties of compounds (E) and (F) significantly influence their reactivity and thus the sensor performance. Compound (E) contains a bulky naphthyl group and a long ethoxyethanol chain, which introduces substantial steric hindrance around the amino group. This reduces the accessibility of the amine site, leading to diminished diazotization efficiency and a weaker response to  $\text{NO}_2^-$ . Conversely, compound (F), with a simpler structure, facilitates a more efficient coupling reaction with the diazonium salt, forming the (CF) azo dye with a more intense colorimetric response. This observation is supported by the lower limit of detection (LOD) and higher binding constant obtained for sensor (CF). DFT calculations further clarify this behavior: compound (F) exhibits a smaller HOMO–LUMO gap (3.05 eV) than (E) (3.07 eV) (Fig. 9), indicating enhanced reactivity and better electron transfer efficiency in F due to its primary amine and naphthyl ring. In contrast, the ethoxyethanol chain in (E) is less electron-donating than (F)'s ethylenediamine moiety (Fig. S22, ESI<sup>†</sup>), resulting in reduced electron density on the amino group and a larger HOMO–LUMO gap, thereby decreasing its reactivity.

Moreover, ESP (electrostatic potential) mapping (Fig. S22, ESI<sup>†</sup>) reveals a more concentrated negative potential around the para-nitrogen of compound (F), which enhances its

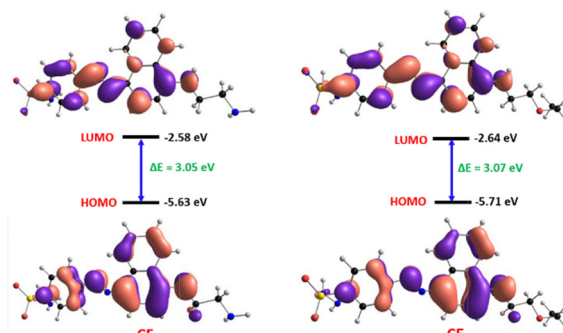


Fig. 9 Energy profile diagram of azo dye products CF and CE.



interaction with the diazonium intermediate and stabilizes the transition state during the coupling reaction. On the other hand, the ESP map of (E) shows a more diffuse electron distribution, and the steric bulk of the ethoxyethanol chain further hinders effective coupling. The presence of the ethoxy group also likely introduces electron polarization, withdrawing electron density from the nucleophilic site, and thereby reducing the compound's reactivity. The optimized structure and calculated electrostatic surfaces of the synthesized azo-dyes are depicted in Fig. S23 (ESI†).

The formation of the azo dyes (CE) and (CF) was further confirmed by FT-IR and LC-MS analyses. FT-IR spectra (Fig. S24, ESI†) revealed the disappearance of amidogen vibrations at 3200 and 3343  $\text{cm}^{-1}$  in compound (C)<sup>40</sup> after reaction with (E) or (F), accompanied by the appearance of a new weak peak at  $\sim 1460 \text{ cm}^{-1}$  corresponding to  $\text{N}=\text{N}$  stretching, confirming azo dye formation.<sup>51</sup> The LC-MS spectra (Fig. S25, ESI†) showed peaks at  $m/z$  429.35 (Fig. S25a, ESI†) and 385.35 (Fig. S25b, ESI†), affirming the molecular weights of the (CE) and (CF) azo dyes, respectively.

For  $\text{NO}_3^-$  detection, the sensing mechanism involves its reduction to  $\text{NO}_2^-$  using Zn dust, as shown in Scheme 3. Zn acts as the reducing agent and gets oxidized to  $\text{Zn}^{2+}$ . Again, compound (F) forms a complex with the resultant  $\text{Zn}^{2+}$ .<sup>52</sup> Interestingly, DFT studies demonstrated that both (E) and (F) can coordinate with  $\text{Zn}^{2+}$ , forming  $\text{E@Zn}$  and  $\text{F@Zn}$  complexes that enhance  $\text{NO}_3^-$  reduction efficiency (Fig. S26, ESI†). Notably, the  $\text{E@Zn}$  complexes exhibited lower HOMO–LUMO gaps (4.31 and 4.35 eV) than  $\text{F@Zn}$  (4.46 eV), indicating higher complex stability. This can be attributed to the bidentate coordination sites provided by (E)—either N, O, or O, O pairs—which interact more strongly with  $\text{Zn}^{2+}$  compared to the N,N bidentate site of (F). Literature reports also confirm that Zn–O bonds are more stable than Zn–N bonds.<sup>53</sup> Thus, the superior stability of  $\text{E@Zn}$  complexes increases the availability of  $\text{NO}_2^-$  in the medium, enhancing the  $\text{NO}_3^-$  sensing capability of (CE). Therefore, between the two azo dye-based sensors, (CF) demonstrated superior sensitivity and selectivity for  $\text{NO}_2^-$  detection due to better coupling efficiency and electron transfer, whereas (CE) exhibited enhanced performance in  $\text{NO}_3^-$  sensing, primarily due to its stronger and more stable complexation with  $\text{Zn}^{2+}$ , which facilitated more effective  $\text{NO}_3^-$  reduction to  $\text{NO}_2^-$ .

### 3.6. Real-time applications

**3.6.1. Smartphone assisted  $\text{NO}_2^-$  sensing.** We have developed a smartphone-based colorimetric sensor to detect  $\text{NO}_2^-$  in aqueous medium based on the various color forms associated with changing  $\text{NO}_2^-$  concentrations. The RGB (red, green, and blue) value was measured by gradually adding  $\text{NO}_2^-$  solution into the dye. The  $\text{NO}_2^-$  concentration was varied from 0 to 0.29 mM. Fig. 10 demonstrates a R + G + B intensity value for different  $\text{NO}_2^-$  concentrations for both of the chemosensors (CE) and (CF). With correlation values ( $R^2$ ) of 0.87 and 0.98, respectively, the chemosensors (CE) and (CF) both displayed a linear fitting curve (Fig. 10a and b). This finding concludes that

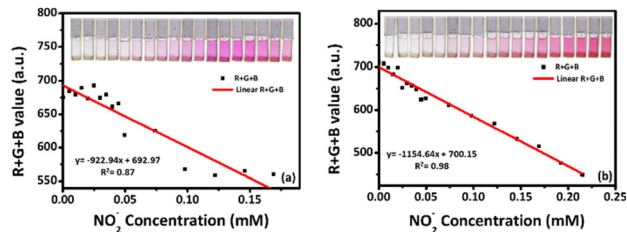


Fig. 10 Smartphone-assisted colorimetric detection of  $\text{NO}_2^-$  ion calibration plot for sensor (a) (CE) and (b) (CF).

Android mobile phone-assisted color software can afford a  $\text{NO}_2^-$  detecting system in real samples. It should be noted that since different manufacturing companies and models utilize different light sources, this calibration curve may vary among Android mobile phones. Therefore, any common gadget, such as an Android smartphone, might be used to quantitatively detect  $\text{NO}_2^-$ .

**3.6.2. Testing with test strips.** Simple, inexpensive, and dependable colorimetric paper-based test strips were developed for the detection of  $\text{NO}_2^-$  in order to validate the practical application of our suggested sensors by visual identification. The test strips were prepared by drop-casting the dye solution (compounds C and E or compounds C and F with itaconic acid) onto Whatman filter paper and allowing them to air-dry. Later, the test strips were coated with 1 mM aqueous solution of different anions and allowed to dry. The color of the test strips was changed from colorless to pink in the case of  $\text{NO}_2^-$ , which is depicted in Fig. 11 [in the case of the sensor (CE) and sensor (CF)]. Moreover, test strips with different concentrations of  $\text{NO}_2^-$  were also prepared with our sensing systems, and the results are depicted in Fig. S27 (ESI†). The chemosensor (CE) demonstrated that with the increase of the  $\text{NO}_2^-$  concentration, the color intensity of the test strips was found to be increased and the highest intensity color was obtained at 8 mM concentration of  $\text{NO}_2^-$ . However, with the further increase of  $\text{NO}_2^-$  concentration, the color intensity was found to be quenched (Fig. S27, ESI†). For sensor (CF) a similar type of observation was noticed and the highest intensity test strips were noticed at a 6 mM concentration of  $\text{NO}_2^-$  (Fig. S27, ESI†). Therefore, this solid-state approach provides a convenient and cost-effective way to detect  $\text{NO}_2^-$  ions with the naked eye.

### 3.7. Real sample analysis

To check the practicability of the sensor towards  $\text{NO}_2^-$ , different types of vegetables such as cabbage, radish, spinach,

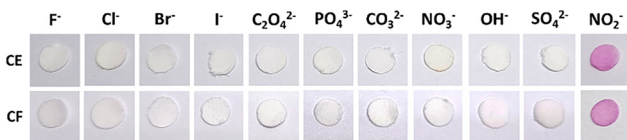


Fig. 11 Photograph of sensing with test strips for sensor (a) (CE) and (b) (CF) in the presence of different anions coated with 1 mM aqueous solution.



lettuce, potato, carrot, and capsicum bought from local shops were tested based on colorimetric readout, and the results are listed in Table S1 (ESI†). Lake water and tap water were also taken for analysis. The samples were spiked with  $\text{NO}_2^-$  to make them 5 mM concentration and four different volumes (50  $\mu\text{L}$ , 100  $\mu\text{L}$ , 150  $\mu\text{L}$ , and 200  $\mu\text{L}$ ) of solution were added into the two different combinations of the sensor system, and their respective absorbance response was noted. The testing results are listed according to the calibration obtained from the respective titration. Here, both the chemosensors demonstrated good recoveries ranging from 93.73% to 106.86%. Hence, both sensors could be used for  $\text{NO}_2^-$  detection.

Table S2 (ESI†) presents the results of a quantitative estimation of  $\text{NO}_3^-$  using our chemosensors in the same set of samples. The samples were spiked with  $\text{NO}_3^-$  to make them 5 mM in concentration. A total of three different concentrations of stock solution were added and the UV-vis response was noted for the sensor (CE). The chemosensor (CE) demonstrated a moderate recovery ranging from 73% to 123.2%. Hence, our proposed chemosensor could be used for  $\text{NO}_3^-$  sensing. For the present investigation, we used only sensor (CE), as in the interference study, the other system (CF) did not provide satisfactory results.

Overall, our proposed chemosensors demonstrate high sensitivity and selectivity for both nitrite and nitrate detection. A comparative analysis with recently reported sensing systems, summarized in Table S3 (ESI†), highlights the importance of our approach. Although the LOD is moderate, it highlights that the sensing system operates effectively in the presence of an organic acid medium, which distinguishes our system from existing methods. Importantly, the chemosensors enable the detection of not only nitrite but also nitrate through an *in situ* reduction process using zinc dust. To further demonstrate practical applicability, we developed a smartphone-assisted detection platform and a portable test kit based on these sensors. The system was successfully validated using real-world samples, including various agricultural products and lake water, confirming its potential for field-level applications.

## 4. Conclusions

In our present study, we successfully developed a pair of colorimetric chemosensors for sensitive and selective detection of  $\text{NO}_2^-$  and  $\text{NO}_3^-$ , utilizing the well-established Griess assay.  $\text{NO}_3^-$  was sensed by converting it to  $\text{NO}_2^-$  in the presence of Zn dust. Both chemosensors formed a different azo-dye upon reaction with  $\text{NO}_2^-$ , resulting in a clear colorimetric response. Itaconic acid was employed as the acidic medium to facilitate the reaction, ensuring optimal conditions for accurate detection. For  $\text{NO}_3^-$  detection,  $\text{NO}_3^-$  was efficiently reduced to  $\text{NO}_2^-$  using Zn dust in the presence of hydrochloric acid, enabling its indirect quantification *via* the same azo-dye reaction. The proposed chemosensors exhibited excellent linearity in response to  $\text{NO}_2^-$  and  $\text{NO}_3^-$  concentrations, with low detection limits highlighting their sensitivity. To explore the practical

application of chemosensors, test strips were fabricated using the synthesized compounds used for designing chemosensors. These strips demonstrated distinct color intensities corresponding to varying concentrations of  $\text{NO}_2^-$ , and the results were further validated using smartphone-assisted colorimetric analysis for real-time and portable monitoring. The reliability of the developed system was confirmed by testing real samples, including various vegetables and lake water, where the sensor displayed excellent recovery rates. This proves the potential of our sensor for environmental and food safety applications, particularly in detecting  $\text{NO}_2^-$  and  $\text{NO}_3^-$  in agricultural products.

In conclusion, the simplicity, sensitivity, and versatility of the proposed colorimetric sensor, combined with its adaptability to test strip formats and smartphone-assisted analysis, make it a promising tool for on-site detection of  $\text{NO}_2^-$  and  $\text{NO}_3^-$ . This work not only advances the utility of Griess assay-based detection systems but also opens new paths for the further development of low-cost, portable, and user-friendly devices for monitoring environmental and food contaminants. The use of monomeric itaconic acid opens the pathway to creating a polymer-based sensor system where a more sensitive system can be designed without the addition of external acid.

## Author contributions

Anubhab Das: writing – original draft, methodology, investigation, software. Sindhu I Sanakal: formal analysis, investigation, software. Gomathi Sivakumar: formal analysis, investigation, software. Anashwara Babu: formal analysis, investigation, writing – review & editing. Samarendra Maji: supervision, conceptualization, writing – review & editing.

## Conflicts of interest

There are no conflicts to declare.

## Data availability

The data used to support the findings of this study are included within the article.

## Acknowledgements

A. D. and S. S. thank SRM IST for providing a fellowship to support the PhD program. S. M. acknowledges SRMIST for providing a seed grant and the Science and Engineering Research Board (SERB), India for a core research grant (CRG/2021/004203). The authors would like to thank Dr Venkatramiah Nutalapati for providing UV-vis spectroscopy.

## References

- 1 L. B. Maia and J. J. G. Moura, How Biology Handles Nitrite, *Chem. Rev.*, 2014, **114**, 5273–5357.



- 2 K. Xiao, R. Tang, J. Wei, J. Wu, Y. Shao, Z. Ma, L. Wang, Z. Hu and Z. Zhou, Achieving stable partial nitrification through synergistic inhibition of free ammonia and salinity on nitrite-oxidizing bacteria, *Front. Environ. Sci. Eng.*, 2025, **19**, 42.
- 3 A. Grzyb, A. Wolna-Maruwka and A. Niewiadomska, The Significance of Microbial Transformation of Nitrogen Compounds in the Light of Integrated Crop Management, *Agronomy*, 2021, **11**, 1415.
- 4 M. Giordano, S. Petropoulos and Y. Rouphael, The Fate of Nitrogen from Soil to Plants: Influence of Agricultural Practices in Modern Agriculture, *Agriculture*, 2021, **11**, 944.
- 5 M. H. Shakil, A. T. Trisha, M. Rahman, S. Talukdar, R. Kobun, N. Huda and W. Zzaman, Nitrites in Cured Meats, Health Risk Issues, Alternatives to Nitrites: A Review, *Foods*, 2022, **11**, 3355.
- 6 M. Karwowska and A. Kononiuk, Nitrates/Nitrites in Food—Risk for Nitrosative Stress and Benefits, *Antioxidants*, 2020, **9**, 241.
- 7 S. Soni, J. W. Anvil, C. Kurian, P. Chakraborty and K. A. Paari, Food additives and contaminants in infant foods: a critical review of their health risk, trends and recent developments, *Food Prod., Process. Nutr.*, 2024, **6**, 63.
- 8 R. M. Keller, L. Beaver, M. C. Prater and N. G. Hord, Dietary Nitrate and Nitrite Concentrations in Food Patterns and Dietary Supplements, *Nutr. Today*, 2020, **55**, 218–226.
- 9 N. S. Bryan, S. Ahmed, D. J. Lefer, N. Hord and E. R. von Schwarz, Dietary nitrate biochemistry and physiology. An update on clinical benefits and mechanisms of action, *Nitric oxide*, 2023, **132**, 1–7.
- 10 M. Norouzzadeh, M. Hasan Rashedi, N. Payandeh, A. Mirdar Harijani and H. Shahinfar, The effects of dietary nitrate on blood pressure and vascular Health: An umbrella review and updated Meta-Analysis and meta-regression, *J. Funct. Foods*, 2024, **114**, 106082.
- 11 M. Volino-Souza, G. V. de Oliveira, V. dos, S. Pinheiro, C. A. Conte-Junior and T. da S. Alvares, The effect of dietary nitrate on macro- and microvascular function: A systematic review, *Crit. Rev. Food Sci. Nutr.*, 2024, **64**, 1225–1236.
- 12 H. N. Rabetafika, A. Razafindralambo, B. Ebenso and H. L. Razafindralambo, Probiotics as Antibiotic Alternatives for Human and Animal Applications, *Encyclopedia*, 2023, **3**, 561–581.
- 13 X. F. Hospital, E. Hierro, J. Arnau, J. Carballo, J. S. Aguirre, M. Gratacós-Cubarsí and M. Fernández, Effect of nitrate and nitrite on *Listeria* and selected spoilage bacteria inoculated in dry-cured ham, *Food Res. Int.*, 2017, **101**, 82–87.
- 14 C. Loffi, M. Cirlini, N. Cavalca, G. Saccani, R. Virgili, G. Galaverna and T. Tedeschi, Changes in proteolysis and volatile fraction of nitrite-free Italian-type salami modified in formulation and processing, *Int. J. Food Sci. Technol.*, 2024, **59**, 5587–5597.
- 15 S. A. Hussain, S. R. Ahmad and H. Fayaz, in *Hand Book of Processed Functional Meat Products*, Springer Nature Switzerland, Cham, 2024, pp. 365–404.
- 16 E. F. Bowles, M. Burleigh, A. Mira, S. G. J. Van Breda, E. Weitzberg and B. T. Rosier, Nitrate: “the source makes the poison”, *Crit. Rev. Food Sci. Nutr.*, 2024, 1–27.
- 17 I. J. Chaudhary, R. Chauhan, S. S. Kale, S. Gosavi, D. Rathore, V. Dwivedi, S. Singh and V. K. Yadav, Ground-water Nitrate Contamination and its Effect on Human Health: A Review, *Water Conserv. Sci. Eng.*, 2025, **10**, 33.
- 18 A. C. da, C. Pinaffi-Langley, H. V. M. Nguyen, D. Whitehead, J. M. Roseland, K. C. Heydorn, X. Wu, P. R. Pehrsson, F. A. Hays and N. G. Hord, Nitrate and nitrite quantification in U.S. vegetable-based baby foods and infant formula via ozone chemiluminescence, *J. Food Compos. Anal.*, 2025, **137**, 106902.
- 19 A. Viancelli and W. Michelon, Climate Change and Nitrogen Dynamics: Challenges and Strategies for a Sustainable Future, *Nitrogen*, 2024, **5**, 688–701.
- 20 C.-Y. Hou, L.-M. Fu, W.-J. Ju and P.-Y. Wu, Microfluidic colorimetric system for nitrite detection in foods, *Chem. Eng. J.*, 2020, **398**, 125573.
- 21 S. S. Paramasivam, S. A. Mariappan, N. K. Sethy and P. Manickam, Enzyme mimetic electrochemical sensor for salivary nitrite detection using copper chlorophyllin and carbon nanotubes-functionalized screen printed electrodes, *Mater. Adv.*, 2023, **4**, 6223–6232.
- 22 P. Lei, N. Wu, Y. Zhou, C. Dong, M. Li and S. Shuang, Simple strategy for dual-responsive ratio electrochemical-colorimetric detection of nitrite in food and environment, *Microchim. Acta*, 2024, **191**, 701.
- 23 P. J. Sephra., C. Tharini, A. Sachdev and E. Manikandan, An efficient sensing system using ion-selective membrane on Ni<sub>2</sub>O<sub>3</sub>/rGO nanocomposite for electrochemical detection of nitrate ions, *J. Alloys Compd.*, 2024, **980**, 173414.
- 24 H. Li, Y. Song, B. Zhou and H. Xu, Nitrite: From Application to Detection and Development, *Appl. Sci.*, 2024, **14**, 9027.
- 25 M. Darestani-Farahani, F. Ma, V. Patel, P. R. Selvaganapathy and P. Kruse, An ion-selective chemiresistive platform as demonstrated for the detection of nitrogen species in water, *Analyst*, 2023, **148**, 5731–5744.
- 26 X. Xia, G. Yang, H. Tian, F. Cao, F. Luo and D. Dong, Development of a rapid sensor system for nitrate detection in water using enhanced Raman spectroscopy, *RSC Adv.*, 2025, **15**, 5728–5736.
- 27 J. Lei, H. Zheng, L. Liu and W. Li, Simultaneous determination of six nitroaromatic compounds and three anions in environmental matrices using a liquid chromatography-ion chromatography coupled system, *Chin. J. Chromatogr.*, 2024, **42**, 92–98.
- 28 Y. Mai, A. Ghiasvand, V. Gupta, S. Edwards, S. Cahoon, K. Debruille, I. Mikhail, E. Murray and B. Paull, Application of a portable ion chromatograph for real-time field analysis of nitrite and nitrate in soils and soil pore waters, *Talanta*, 2024, **274**, 126031.
- 29 N. Luckovitch and E. Pagliano, A reference isotope dilution headspace GC/MS method for the determination of nitrite and nitrate in meat samples, *Int. J. Food Sci. Technol.*, 2020, **55**, 1110–1118.
- 30 H. Kodamatani, S. Kubo, A. Takeuchi, R. Kanzaki and T. Tomiyasu, Sensitive Detection of Nitrite and Nitrate in Seawater by 222 nm UV-Irradiated Photochemical Conversion



- to Peroxynitrite and Ion Chromatography-Luminol Chemiluminescence System, *Environ. Sci. Technol.*, 2023, **57**, 5924–5933.
- 31 M. Zeng, C. Zhang, Q. Yao, J. Jin, T.-X. Ye, X. Chen, Z. Guo and X. Chen, Multifunction nanoenzyme-assisted ion-selective and oxidation catalysis SERS biosensors for point-of-care nitrite testing, *Sens. Actuators, B*, 2024, **405**, 135352.
- 32 Z. Yang, J. Zhang, J. Zhao, W. Zhou, Y. Cheng, Z. Xu, P. Wei, Z. Wang, H. Liang and C. Li, A high-sensitivity lab-on-a-chip analyzer for online monitoring of nitrite and nitrate in seawater based on liquid waveguide capillary cells, *Lab Chip*, 2024, **24**, 3528–3535.
- 33 K. M. Miranda, M. G. Espey and D. A. Wink, A Rapid, Simple Spectrophotometric Method for Simultaneous Detection of Nitrate and Nitrite, *Nitric oxide*, 2001, **5**, 62–71.
- 34 D. Giustarini, I. Dalle-Donne, D. Tsikas and R. Rossi, Oxidative stress and human diseases: Origin, link, measurement, mechanisms, and biomarkers, *Crit. Rev. Clin. Lab. Sci.*, 2009, **46**, 241–281.
- 35 V. M. Ivanov, The 125th Anniversary of the Griess Reagent, *J. Anal. Chem.*, 2004, **59**, 1002–1005.
- 36 E. García-Robledo, A. Corzo and S. Papaspyrou, A fast and direct spectrophotometric method for the sequential determination of nitrate and nitrite at low concentrations in small volumes, *Mar. Chem.*, 2014, **162**, 30–36.
- 37 A. Choodum, J. Tiengtum, T. Taweekarn and W. Wongniramaikul, Convenient environmentally friendly on-site quantitative analysis of nitrite and nitrate in seawater based on polymeric test kits and smartphone application, *Spectrochim. Acta, Part A*, 2020, **243**, 118812.
- 38 Y.-T. Tai, C.-Y. Cheng, Y.-S. Chen and F.-H. Ko, A hydrogel-based chemosensor applied in conjunction with a Griess assay for real-time colorimetric detection of nitrite in the environment, *Sens. Actuators, B*, 2022, **369**, 132298.
- 39 L. Capitán-Vallvey, R. Avidad, M. Fernández-Ramos, A. Ariza-Avidad and E. Arroyo, Test strip for determination of nitrite in water, *Anal. Bioanal. Chem.*, 2002, **373**, 289–294.
- 40 H. Wu, X. Shen, D. Huo, Y. Ma, M. Bian, C. Shen and C. Hou, Fluorescent and colorimetric dual-readout sensor based on Griess assay for nitrite detection, *Spectrochim. Acta, Part A*, 2020, **225**, 117470.
- 41 M. K. Morsy, O. M. Morsy, E. M. Abd-Elaaty and R. Elsabagh, Development and Validation of Rapid Colorimetric Detection of Nitrite Concentration in Meat Products on a Polydimethylsiloxane (PDMS) Microfluidic Device, *Food Anal. Methods*, 2022, **15**, 552–564.
- 42 T. J. Chow and M. S. Johnstone, Determination of nitrate in sea water, *Anal. Chim. Acta*, 1962, **27**, 441–446.
- 43 T. Jiwrungrueangkul, O. Kongpuen, M. Yucharoen, C. Sangmanee, D. Tipmanee, T. Areerob and P. Sompongchiyakul, Modification and validation of an analytical method for the simple determination of nitrate in seawater by reduction to nitrite with zinc powder, *Mar. Chem.*, 2023, **251**, 104235.
- 44 E. Murray, E. P. Nesterenko, M. McCaul, A. Morrin, D. Diamond and B. Moore, A colorimetric method for use within portable test kits for nitrate determination in various water matrices, *Anal. Methods*, 2017, **9**, 680–687.
- 45 S.-C. Pai, Y.-T. Su, M.-C. Lu, Y. Chou and T.-Y. Ho, Determination of Nitrate in Natural Waters by Vanadium Reduction and the Griess Assay: Reassessment and Optimization, *ACS ES&T Water*, 2021, **1**, 1524–1532.
- 46 K. R. Kunduru, A. Basu, T. Tsah and A. J. Domb, Polymer with pendant diazo-coupling functionality for colorimetric detection of nitrates, *Sens. Actuators, B*, 2017, **251**, 21–26.
- 47 N. Devi, S. Singh, S. Manickam, N. Cruz-Martins, V. Kumar, R. Verma and D. Kumar, Itaconic Acid and Its Applications for Textile, Pharma and Agro-Industrial Purposes, *Sustainability*, 2022, **14**, 13777.
- 48 S. V. Bukharov, A. R. Burilov, R. G. Tagasheva, G. N. Nugumanova, E. V. Nikitina and N. A. Mukmeneva, Synthesis and Antibacterial Activity of Sulfanilamides Containing Sterically Hindered Phenol Fragments, *Russ. J. Org. Chem.*, 2021, **57**, 1621–1627.
- 49 H. Guo, Y. Zhuang, J. Cao and G. Zhang, Green and Efficient Protocol for the Synthesis of N-(2-Hydroxyethyl)anilines by the Alkylation Reaction in Ionic Liquid, *Synth. Commun.*, 2014, **44**, 3368–3374.
- 50 S. Luetic, Z. Knezovic, K. Jurcic, Z. Majic, K. Tripkovic and D. Sutlovic, Leafy Vegetable Nitrite and Nitrate Content: Potential Health Effects, *Foods*, 2023, **12**, 1655.
- 51 F. Zimmermann, T. Lippert, C. Beyer, J. Stebani, O. Nuyken and A. Wokaun, N=N Vibrational Frequencies and Fragmentation Patterns of Substituted 1-Aryl-3,3-Dialkyl-Triazenes: Comparison with other High-Nitrogen Compounds, *Appl. Spectrosc.*, 1993, **47**, 986–993.
- 52 M. S. Refat, A. M. A. Adam, T. Sharshar, H. A. Saad and H. H. Eldaroti, Utility of positron annihilation lifetime technique for the assessment of spectroscopic data of some charge-transfer complexes derived from N-(1-Naphthyl)ethylenediamine dihydrochloride, *Spectrochim. Acta, Part A*, 2014, **122**, 34–47.
- 53 Z.-Q. Liu, Y. M. Ng, P. J. Tiong, R. A. Abu Talip, N. Jasin, V. Y. M. Jong and M. G. Tay, Five-Coordinate Zinc(II) Complex: Synthesis, Characterization, Molecular Structure, and Antibacterial Activities of Bis-[(E)-2-hydroxy-N'-(1-(4-methoxyphenyl)ethylidene)benzohydrazido]dimethylsulfoxidezinc(II) Complex, *Int. J. Inorg. Chem.*, 2017, **2017**, 1–8.

